Direct imaging discovery of a young giant planet orbiting on Solar System scales

Stolker, T.; Samland, M.; Waters, L.B.F.M.; Ancker, M.E. van den; Balmer, W.O.; Lacour, S.; ... ; Yazici, S.

A&A, 700, A21 (2025)
https://doi.org/10.1051/0004-6361/202555064

Astronomy & Astrophysics

Direct imaging discovery of a young giant planet orbiting on Solar System scales

T. Stolker[1,⋆], M. Samland[2], L. B. F. M. Waters[3], M. E. van den Ancker[4], W. O. Balmer[5,6], S. Lacour[7,4], M. L. Sitko[8], J. J. Wang[9], M. Nowak[10], A.-L. Maire[11], J. Kammerer[4], G. P. P. L. Otten[12], R. Abuter[4], A. Amorim[16,17], M. Benisty[2], J.-P. Berger[11], H. Beust[11], S. Blunt[9], A. Boccaletti[7], M. Bonnefoy[11], H. Bonnet[4], M. S. Bordoni[18], G. Bourdarot[18], W. Brandner[2], F. Cantalloube[11], P. Caselli[18], B. Charnay[7], G. Chauvin[19], A. Chavez[9], A. Chomez[7,11], E. Choquet[20], V. Christiaens[21], Y. Clénet[7], V. Coudé du Foresto[7], A. Cridland[1], R. Davies[18], R. Dembet[7], J. Dexter[8], C. Dominik[13], A. Drescher[18], G. Duvert[11], A. Eckart[22,23], F. Eisenhauer[18], N. M. Förster Schreiber[18], P. Garcia[17,24], R. Garcia Lopez[25,2], T. Gardner[26], E. Gendron[7], R. Genzel[18,27], S. Gillessen[18], J. H. Girard[6], S. Grant[18], X. Haubois[28], G. Heißel[29,7], Th. Henning[2], S. Hinkley[30], S. Hippler[2], M. Houllé[19], Z. Hubert[11], L. Jocou[11], M. Keppler[2], P. Kervella[7], L. Kreidberg[2], N. T. Kurtovic[18], A.-M. Lagrange[11,7], V. Lapeyrère[7], J.-B. Le Bouquin[11], D. Lutz[18], F. Mang[18], G.-D. Marleau[31,32,2], A. Mérand[4], M. Min[14], P. Mollière[2], J. D. Monnier[33], C. Mordasini[32], D. Mouillet[11], E. Nasedkin[2], T. Ott[18], C. Paladini[28], T. Paumard[7], K. Perraut[11], G. Perrin[7], O. Pfuhl[4], N. Pourré[11], L. Pueyo[6], S. P. Quanz[15], D. C. Ribeiro[18], E. Rickman[34], Z. Rustamkulov[35], J. Shangguan[38], T. Shimizu[18], D. Sing[5,35], J. Stadler[36,37], O. Straub[37], C. Straubmeier[22], E. Sturm[18], L. J. Tacconi[18], E.F. van Dishoeck[1,18], A. Vigan[20], F. Vincent[7], S. D. von Fellenberg[23], F. Widmann[18], T. O. Winterhalder[4], J. Woillez[4], and S. Yazici[18]

(Affiliations can be found after the references)

Received 7 April 2025 / Accepted 6 June 2025

ABSTRACT

Context. HD 135344 AB is a young visual binary system that is best known for the protoplanetary disk around the secondary star. The circumstellar environment of the A0-type primary star, on the other hand, is already depleted. HD 135344 A is therefore an ideal target for the exploration of recently formed giant planets because it is not obscured by dust.
Aims. We searched for and characterized substellar companions to HD 135344 A down to separations of about 10 au.
Methods. We observed HD 135344 A with VLT/SPHERE in the $H23$ and $K12$ bands and obtained YJ and YJH spectroscopy. In addition, we carried out VLTI/GRAVITY observations for the further astrometric and spectroscopic confirmation of a detected companion.
Results. We discovered a close-in young giant planet, HD 135344 Ab, with a mass of about 10 M_J. The multi-epoch astrometry confirms the bound nature based on common parallax and common proper motion. This firmly rules out the scenario of a non-stationary background star. The semi-major axis of the planetary orbit is approximately 15–20 au, and the photometry is consistent with that of a mid L-type object. The inferred atmospheric and bulk parameters further confirm the young and planetary nature of the companion.
Conclusions. HD 135344 Ab is one of the youngest directly imaged planets that has fully formed and orbits on Solar System scales. It is a valuable target for studying the early evolution and atmosphere of a giant planet that could have formed in the vicinity of the snowline.

Key words. techniques: high angular resolution – planets and satellites: detection – planets and satellites: gaseous planets – stars: individual: HD 135344 A

1. Introduction

HD 135344 AB is a visual binary system that is located in Upper Centaurus Lupus (UCL) region of the Sco-Cen OB association. The secondary F4-type star, HD 135344 B, has been studied for several decades because of its prominent IR excess. During more recent years, the protoplanetary disk was spatially resolved and revealed a central cavity (Brown et al. 2009; Garufi et al. 2013), spiral arms (Muto et al. 2012), and variable shadowing by the inner disk (Stolker et al. 2017). These disk features might indicate planet-disk interactions, but the suspected planets have remained hidden (e.g., Maire et al. 2017; Cugno et al. 2024).

While planet formation appears to be ongoing at HD 135344 B, the circumstellar environment of the A0-type primary star, HD 135344 A, is already largely depleted, given the absence of strong IR excess in the spectral energy distribution (SED). HD 135344 A and B are proper-motion binary partners (Mason et al. 2001) with an angular separation of 21.″2 (≈2800 au), and their circumstellar disks have therefore likely evolved independently, depending on the eccentricity of the orbits. We note that the secondary star has incorrectly been referred to as HD 135344 in some cases, although the issue had already been pointed out by Coulson & Walther (1995).

⋆ Corresponding author.

Table 1. Observation details.

UT date[a]	Instrument	Mode	DIT/NDIT/NEXP[b]	Airmass	Seeing[c] (arcsec)	τ_0[d] (ms)	π[e] (deg)
2019 May 09	SPHERE	IRDIFS	48/3/16	1.02–1.03	0.78 ± 0.09	2.7 ± 0.3	43.8
2019 Jul. 06	SPHERE	IRDIFS	48/3/16	1.02–1.03	0.66 ± 0.10	5.3 ± 0.6	43.3
2021 Jul. 16	SPHERE	IRDIFS	4/32/25	1.02–1.05	0.64 ± 0.11	3.3 ± 0.5	78.3
2022 May 04	SPHERE	IRDIFS_EXT	4/32/24	1.02–1.05	0.84 ± 0.18	4.5 ± 1.0	78.4
2022 Jul. 19	GRAVITY	ON-AXIS	100/4/8	1.03–1.13	1.26 ± 0.19	1.8 ± 0.2	46.0
2023 May 08	GRAVITY	ON-AXIS	100/4/7	1.03–1.13	0.95 ± 0.09	3.6 ± 0.5	35.2
2023 Jul. 01	GRAVITY	ON-AXIS	100/4/4	1.08–1.17	0.79 ± 0.12	6.4 ± 5.2	12.2

Notes. [(a)]UT date at the start of the observations. [(b)]Detector integration time, number of integrations per exposure, and number of exposures. The listed values of the SPHERE observations are taken from IRDIS. [(c,d)]Sample mean and standard deviation of the DIMM seeing and coherence time. [(e)]Rotation by the parallactic angle.

The two stars in the HD 135344 AB binary system are expected to be coeval. The pre-main-sequence age of the secondary star can therefore be adopted as the age of the main-sequence primary star. Garufi et al. (2018) inferred an age of $11.9^{+3.7}_{-5.8}$ Myr for HD 135344 B by using stellar evolutionary tracks and the *Gaia* parallax. In addition to the young age, giant planets on wide orbits are most commonly detected around intermediate-mass stars (e.g., Nielsen et al. 2019; Vigan et al. 2021). The youth, spectral type, and dust-depleted environment make HD 135344 A an excellent target to search for young giant planets.

We report high-contrast imaging observations with which we explore the circumstellar environment of HD 135344 A for the first time. We discovered a young giant planet that we confirmed through a detailed astrometric and spectral analysis. The evidence for the bound and planetary nature accumulated based on the observations and results. For simplicity, we refer to the discovered source as HD 135344 Ab from here on.

2. Observations and data reduction

2.1. VLT/SPHERE high-contrast imaging

HD 135344 A was observed with VLT/SPHERE (Beuzit et al. 2019) on the nights of 2019 May 8, 2019 July 5, 2021 July 16, and 2022 May 3. The first observations were carried out with the `IRDIFS` mode so that we could benefit from the highest angular resolution. We used the IRDIS dual-band camera with the *H*23 filters (Dohlen et al. 2008; Vigan et al. 2010), and we obtained a low-resolution *YJ* spectrum ($R \approx 50$) with IFS (Claudi et al. 2008). The first observation, which led to the discovery, did not fully meet the requested conditions (and hence, it was repeated in July), but the quality was sufficient for a robust detection. We then repeated the observation in 2021 to confirm the source at the same wavelength. In 2022, we used the `IRDIFS_EXT` mode to obtain *K*12 dual-band imaging and a low-resolution *YJH* spectrum ($R \approx 30$).

The integration times and observing conditions are listed in Table 1. We used deep exposures with a detector integration time (DIT) of 48 and 64 seconds for the simultaneous IRDIS and IFS measurements, respectively, in 2019. After we detected the source at a small separation, we decided to change the observing strategy. Specifically, we used a DIT of 4 and 6 seconds for IRDIS and IFS, respectively, to sample the speckle variation on a faster timescale, which is beneficial for the post-processing. We also left the satellite spots on throughout the observations to enable a more accurate centering and flux calibration.

The IRDIS and IFS data were reduced with `vlt-sphere`[1] (Vigan 2020), which provides a Python wrapper for the `EsoRex` recipes. It also applies a recalibration of the IFS wavelength solution, and it centers the coronagraphic frames based on the satellite spots. We post-processed the IRDIS data with `PynPoint`[2] by applying full-frame principal component analysis (PCA) to subtract the stellar halo and speckles (Amara & Quanz 2012; Stolker et al. 2019). For the astrometric and photometric measurements, we followed the procedure outlined by Stolker et al. (2020), which corrects for self-subtraction and includes the systematic uncertainty in the error budget. The extracted fluxes were corrected for the coronagraph throughput, which ranged from 97% to 93% as the separation of the planet decreased.

The IFS data were post-processed with `TRAP`[3], which specifically is a more powerful detection and calibration technique for sources at small separation because systematics are modeled in the temporal instead of the spatial domain (Samland et al. 2021). We analyzed the *YJ* and *YJH* spectra from 2021 and 2022, respectively, because these datasets were obtained with continuous satellite spots. Similar to the IRDIS data, the amplitudes of the spots were used to identify low-quality frames and their temporal variation was accounted for in the spectral extraction. The wavelength-averaged S/N of the discovered source is 2.9 and 1.5 for the *YJ* and *YJH* spectra, respectively. The higher S/N of the *YJ* spectrum might be due to the better seeing conditions.

The contrasts were converted into magnitudes and fluxes by using a synthetic stellar spectrum and a flux-calibrated spectrum of Vega (Bohlin et al. 2014). Table A.1 in Appendix A lists the inferred stellar parameters and the synthetic magnitudes of HD 135344 A in the IRDIS filters that were computed from the posterior distributions. The synthetic IFS spectrum of HD 135344 A was extracted by sampling random spectra from the posterior, smoothing them to $R = 30$, and rebinning to the wavelength solution of the instrument.

2.2. VLTI/GRAVITY dual-field interferometry

The system was also observed with the four unit telescopes (UTs) of VLTI/GRAVITY on the nights of 2022 July 19, 2023 May 8, and 2023 July 1 (see Table 1). GRAVITY provides exquisite astrometric precision for directly imaged planets and

[1] https://github.com/avigan/SPHERE
[2] https://github.com/PynPoint/PynPoint
[3] https://github.com/m-samland/trap

medium-resolution ($R \approx 500$) K-band spectroscopy (GRAVITY Collaboration 2017). We used the dual-field on-axis mode with the fringe-tracking fiber centered on the star and the science fiber alternating between the star and planet. This strategy enables referencing and accurate calibration of the interferometric visibilities (GRAVITY Collaboration 2020; Lacour et al. 2020). For the third observation, we benefitted from the recently commissioned faint mode, which turns the metrology lasers off during the science exposures. This yields a detection with a higher S/N of faint companions (Widmann et al. 2022).

Standard data reduction procedures were applied with the `run_gravi_reduce` script[4] that calls the `EsoRex` recipes. We then used the `exoGravity`[5] pipeline for phase referencing, subtracting the stellar component from the visibilities, and extracting the astrometry and spectrum (GRAVITY Collaboration 2019, 2020; Nowak et al. 2020). After calibrating the full datasets, we excluded the baselines of UT3 from the 2023 May data because of an issue with the metrology. The wavelength-averaged S/N of the spectra of the discovered source is 1.1, 2.6, and 5.0 (in chronological order). We only included the GRAVITY spectrum from 2023 July in the analysis because a covariance-weighted combination with the other two spectra did not improve the S/N, in particular, because the systematics in these two spectra are stronger. Similar to the IFS flux calibration, we used a synthetic spectrum to convert the contrast spectrum into fluxes while taking the uncertainties on the stellar spectrum into account.

3. Results

3.1. Direct detection of a young giant planet

The residuals of the PSF subtraction from the imaging observations with SPHERE are shown in Fig. 1. In 2019, we detected an off-axis point source, HD 135344 Ab, which is located west of the star at an approximate separation of $4\lambda/D$ in $H23$. In 2021, the source was detected again, but at a somewhat smaller separation, and in 2022, it was also detected with the $K12$ filters. The PSF shape is typical for a post-processed point source. The negative lobes are due to the inherent self-subtraction effect by angular differential imaging (ADI). The source clearly stands out against the fainter speckle field in the background and is detected with S/N $\approx$ 10 in all IRDIS imaging data. We did not detect extended emission in the data, indicating that the circumstellar environment is indeed depleted in small dust. A feature is also visible in the IRDIS image from 2019 May in the eastward direction, at a separation of $2.5\lambda/D$ from the star. It appears to be noisier than HD 135344 Ab and self-subtracts more quickly with an increasing number of components. Two months later, it was no longer detected, suggesting it was likely a speckle residual, as neither a background star nor a planet could have moved enough to become obscured by the coronagraph.

The SPHERE data were not fully conclusive for a confirmation that the discovered source was bound to HD 135344 A. We therefore decided to follow it up with the GRAVITY instrument. Figure 2 shows the detection maps of the GRAVITY observations. The planet is clearly detected in all datasets. We adopted the feature with the highest $\Delta\chi^2$ as the position of the planet, and the contrast spectrum was also extracted at this position. The pattern and elongated shapes in the detection maps depend on the coverage of the (u, v) plane (i.e., the UT baselines and field rotation). For the observation in 2022, the pointing of the fiber was 13.5 mas south of the actual location of the planet, which resulted in a fiber coupling efficiency of 0.89. For the other two observations, the fiber position was (almost) spot-on with the planet due to the improved orbital constraint.

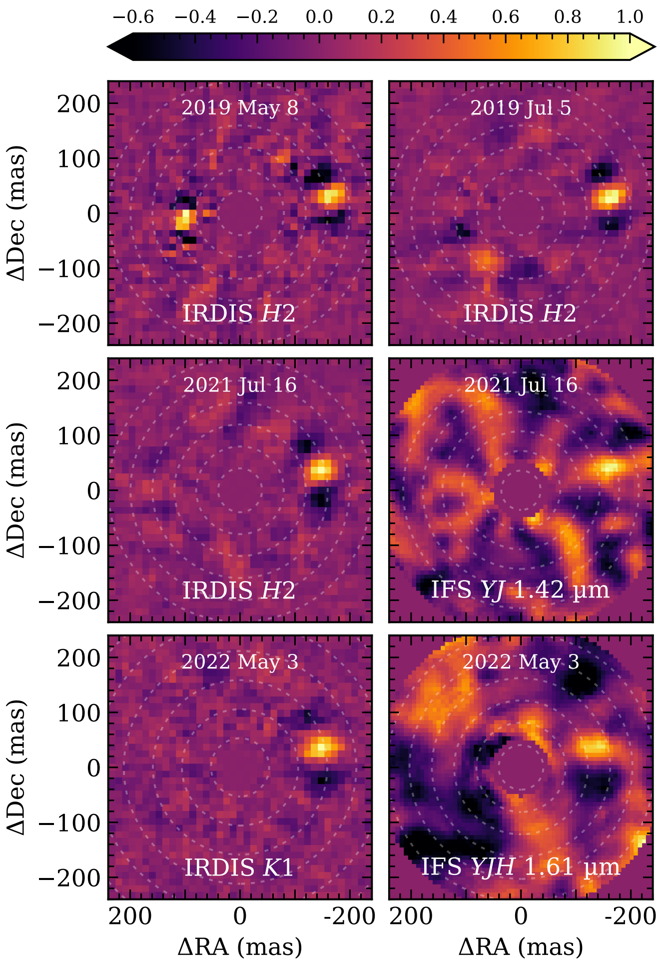

Fig. 1. Detections of HD 135344 Ab with VLT/SPHERE. For IRDIS, the images show the residuals from the PSF subtraction for one of the dual-band filters. For IFS, the images show the detection maps for one of the wavelength channels. The planet is seen in westward direction (i.e., toward the right). The color scale is linear and normalized to the brightest pixel in each image. The dotted circles indicate the separation from the central star in integer multiples of λ/D. The night of the observation is given in each panel.

3.2. Relative astrometry: Planet or background star?

HD 135344 AB is located in the Sco-Cen OB association, which is close to the direction of the Galactic center. There are typically several, if not many, background sources in the $12'' \times 12''$ field of view of the IRDIS camera. In addition to the inner source identified in Sect. 3.1, we detected four more sources. We extracted their astrometry by directly fitting a 2D Gaussian model to the sources in the derotated frames.

The astrometric measurements of HD 135344 Ab are listed in Table 2 and are shown in Fig. 3 together with the suspected background sources. This figure displays the astrometry relative to the first epoch and shows that the planet moves mostly eastward,

[4] https://www.eso.org/sci/facilities/paranal/instruments/gravity/tools.html
[5] https://gitlab.obspm.fr/mnowak/exogravity

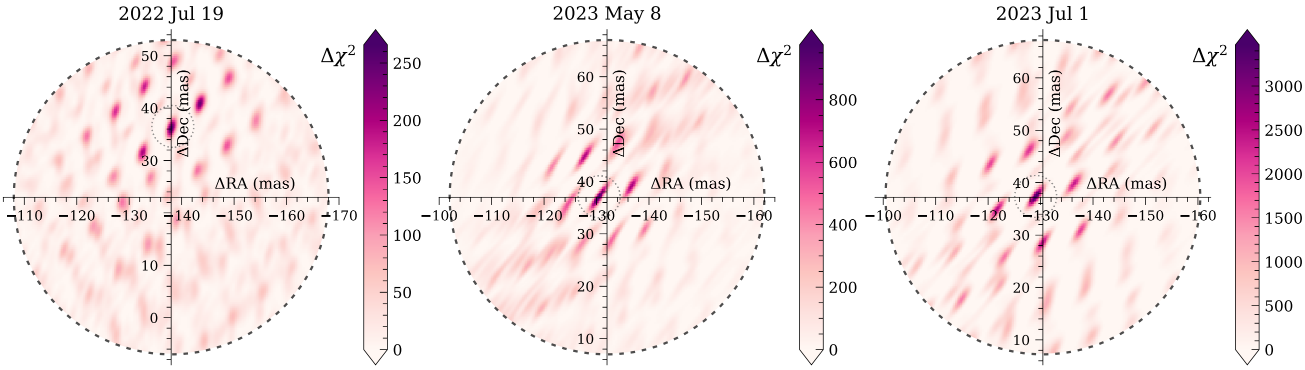

Fig. 2. Detections of HD 135344 AB with VLTI/GRAVITY. The color scale of the detection maps shows $\Delta\chi^2 = \chi_{\rm no\,planet} - \chi_{\rm planet}$. The intersection of the axes is at the center of the fiber, which has a field of view of ≈60 mas. For each observation, the feature with the highest likelihood is encircled, which corresponds to the planet position. The night of the observations is shown at the top of each panel.

Table 2. Astrometry of HD 135344 Ab.

UT date[a]	MJD	Instrument	ΔRA[b] (mas)	ΔDec[c] (mas)	ρ^d
2019 May 09	58612.2	SPHERE/IRDIS	−161.6 ± 2.7	31.6 ± 1.3	−0.33
2019 Jul. 06	58670.0	SPHERE/IRDIS	−162.0 ± 2.0	28.2 ± 1.3	−0.17
2021 Jul. 16	59412.0	SPHERE/IRDIS	−144.8 ± 1.9	36.1 ± 1.2	−0.22
2022 May 04	59703.2	SPHERE/IRDIS	−142.3 ± 5.2	35.8 ± 2.0	−0.58
2022 Jul. 19	59779.06	GRAVITY	−138.21 ± 0.15	36.34 ± 0.17	−0.58
2023 May 08	60072.15	GRAVITY	−130.41 ± 0.20	37.00 ± 0.28	−0.95
2023 Jul. 01	60126.98	GRAVITY	−129.07 ± 0.13	37.36 ± 0.08	−0.97

Notes. [(a)]UT date at the start of the observations. [(b,c)]Coordinates, RA and Dec, relative to the star HD 135344 A. [(d)]The Pearson correlation coefficient, ρ, quantifies the correlation between the uncertainties of ΔRA and ΔDec.

whereas the background sources move northeast. The direction of the background sources matches the stationary track, but it shows that the proper motions of the background sources are not negligible. This is also seen in the sample of *Gaia* sources, from which we adopted the proper motions to create a sample of non-stationary background stars.

From this comparison, we conclude that the relative astrometry of the IRDIS background sources is approximately consistent with the population of *Gaia* sources. We did not take differences in the parallax into account, which we expect to be the reason that the IRDIS background sources do not match the bulk of the *Gaia* sources exactly. There might also be systematics in the astrometry, such as the true north uncertainty, which affects sources far from the on-axis science target more strongly.

The planet appears to move distinctly from the background sources, although somewhat in the same direction. This initially seemed suspicious. For the last epoch, the simulated positions of the bulk of the *Gaia* sources differ by more than 100 mas from the position of the planet. The sample includes however a few outliers for which the magnitude and direction of the proper motions are similar to HD 135344 A. This yields a probability of ≈0.1% that the putative planet instead is a background star with an unusually high proper motion. It is important to consider and rule out a peculiar proper motion scenario, as was shown by Nielsen et al. (2017) for the case of HD 131399 A.

3.3. Ruling out a non-stationary background star

The analysis in Sect. 3.2 showed that the astrometric measurements are difficult to explain with a background star. In this section, we statistically explore the scenario of a background (or foreground) object by fitting the relative astrometry of HD 135344 Ab with a non-stationary background model. We used `backtracks`[6] (Balmer et al. 2025) to determine the coordinates, proper motion, and parallax that best describe the astrometry as a background object. The code uses dynamic nested sampling with the `dynesty` package (Speagle 2020) to estimate the parameter posteriors. At the start, the *Gaia* catalog is queried for the parallaxes and proper motions of sources within a window of 0.2 deg centered on HD 135344 A, and these are used as priors with the Bayesian inference, $\varpi_{Gaia} = 0.4 \pm 0.8$ mas, $\mu_{{\rm RA},Gaia} = -5.1 \pm 5.6$ mas yr^{-1}, and $\mu_{{\rm Dec},Gaia} = -3.8 \pm 4.2$ mas yr^{-1}. We note that a similar sample was used for the proper motions applied in Fig. 3.

Figure 4 shows a random selection of posterior background tracks in comparison with the astrometry. The tracks are close to linear because the inferred parallax, $\varpi = 7.5 \pm 0.1$ mas, of the modeled background source is consistent with the parallax of HD 135344 Ab, $\varpi_* = 7.41 \pm 0.04$ mas. This result is in particular driven by the linear displacement of the GRAVITY astrometry, which was obtained about two months apart. Specifically, the high-precision measurements rule out a helix shape due to a heliocentric parallax of a background star. This is the first confirmation of a directly imaged planet by a common parallax to our knowledge.

The retrieved proper motion, $\mu_{\rm RA} = -9.0 \pm 0.1$ and $\mu_{\rm Dec} = -22.9 \pm 0.1$ mas yr^{-1}, further confirms that the object is

[6] https://github.com/wbalmer/backtracks

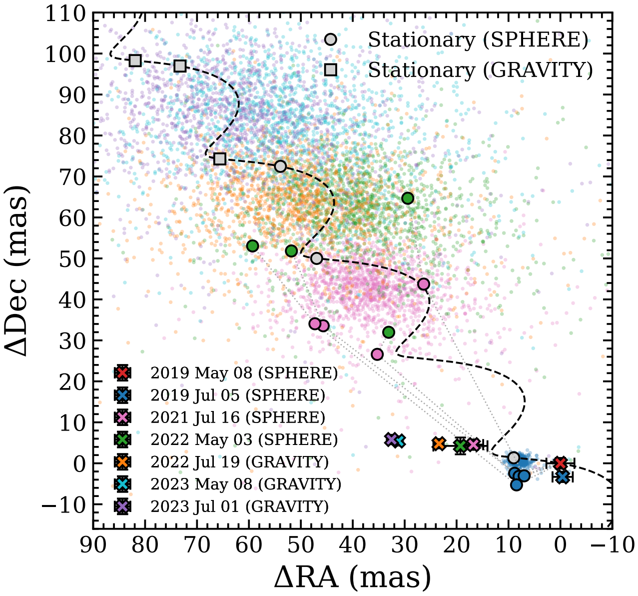

Fig. 3. Astrometric measurements relative to the first epoch. The crosses show the positions of HD 135344 Ab, which moves eastward. The colored circles show the positions of the suspected background sources in the IRDIS field of view, which are connected with dotted lines between epochs. The dashed line shows the track for a stationary background source, and the gray circles and squares indicate the three SPHERE and three GRAVITY epochs, respectively, after the initial detection. The small dots represent a sample of *Gaia* sources within 0.1 deg from HD 135344 A (see main text for details). The colors indicate a specific epoch, for example, all pink markers correspond to 2021 Jul. 16.

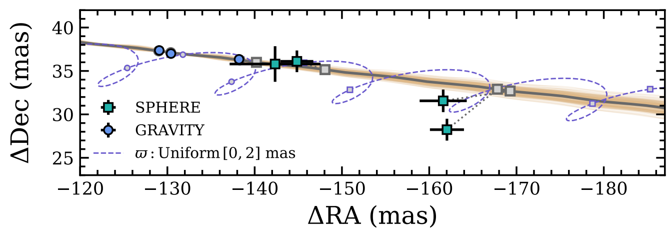

Fig. 4. Background fit of the relative astrometry. The figure shows 200 randomly drawn background tracks from the posterior. The track calculated from the median parameters is shown as the solid gray line. The astrometric measurements are shown with colored markers, and their respective epochs of the best-fit model are shown with gray markers. For comparison, the dashed blue line shows the best-fit model for a parallax prior that forces the source to the background (≥500 pc).

comoving with HD 135344 A. While μ_{RA} is consistent with the prior distribution from *Gaia*, which is also shown in Fig. 3, μ_{Dec}, on the other hand, is a 4.5σ outlier with respect to the *Gaia* sources. Therefore, the analysis shows that the object is most consistent with the proper motion of HD 135344 A. The difference is attributed to the orbital motion, which is approximately linear in the eastward direction. The background fit used the proper motion parameter to mimic the orbital movement, which caused the difference in particular to the RA component of the stellar proper motion, $\mu_{\mathrm{RA},*} = -18.74 \pm 0.05$ mas yr^{-1} and $\mu_{\mathrm{Dec},*} = -24.01 \pm 0.04$ mas yr^{-1} (Gaia Collaboration 2023).

To further quantify the significance, we list in Table 3 the Bayesian evidence (i.e., the marginalized likelihood), $\ln \mathcal{Z}$, for three cases of the background fit. For the stationary model, we fixed the parallax and proper motion to zero. The parameter estimation informed by the *Gaia* priors is the fit that

Table 3. Bayesian evidence.

Model	$\ln \mathcal{Z}$
Keplerian orbit	-34.6 ± 0.1
Background: uniform priors	-64.6 ± 0.2
Background: *Gaia* priors	-81.9 ± 0.2
Background: stationary	-272642.7 ± 0.1

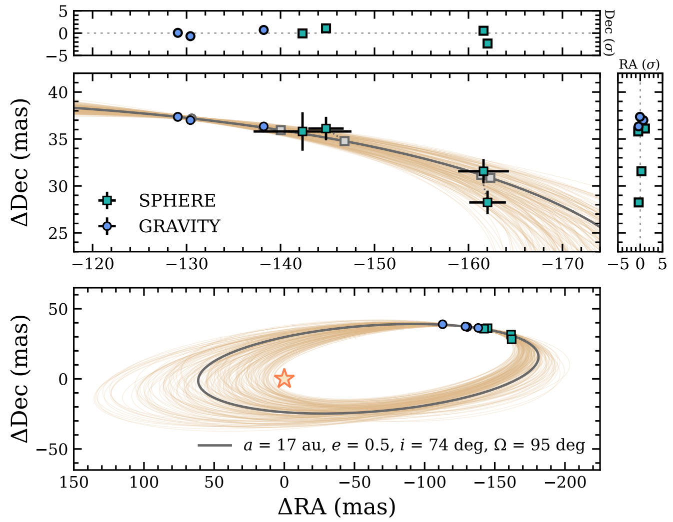

Fig. 5. Orbit fit of the relative astrometry. The bottom panel shows the full orbits, and the top panel shows a zoom of the observation epochs. Both panels show the same 200 orbit samples that were randomly drawn from the posterior. The orbit with the highest likelihood is shown as the solid gray line, and the residuals of the best fit are normalized by the data uncertainties. The astrometric measurements are shown with colored markers, and their respective epochs of the best-fit model are shown with gray markers and are connected with dotted lines. The planet moves in counterclockwise direction.

we described earlier in this section. For comparison, loosening the priors to uniform distributions increases $\ln \mathcal{Z}$ because the measurements did not match the bulk of the *Gaia* sample. Instead, as we describe in the next section in more detail, the Bayes factor of the model comparison between the orbit and background fit is $\Delta \ln \mathcal{Z} \geq 30$. We therefore conclude that the evidence is strong that the source is comoving with and orbiting HD 135344 A.

3.4. Orbital analysis

The discovered planet shows clear orbital movement, possibly even with a slight curvature. We therefore carried out a fit with `orbitize!`[7] (Blunt et al. 2020) to infer its orbital elements. The posterior distributions were sampled with the nested sampling algorithm from `MultiNest` (Feroz & Hobson 2008; Buchner et al. 2014) while marginalizing over the parallax and system mass (see Table A.1). We used 2000 live points and restricted the priors on the argument of periastron, ω, and longitude of the ascending node, Ω, to one of the two solutions.

Figure 5 shows the posterior orbits, and the credible regions are provide in Table 5. We retrieved a semi-major axis of $a = 16.5^{+2.8}_{-2.0}$ au, which corresponds to a period of $P = 45^{+11}_{-8}$ yr. The eccentricity is hardly constrained and is negatively

[7] https://github.com/sblunt/orbitize

Table 4. Photometry of HD 135344 Ab.

UT date	Filter	Contrast (mag)	App. magnitude (mag)	Flux ($\mathrm{W\,m^{-2}\,\mu m^{-1}}$)
2019 May 09	IRDIS $H2$	10.17 ± 0.10	17.76 ± 0.11	$1.02 \pm 0.10 \times 10^{-16}$
	IRDIS $H3$	10.05 ± 0.12	17.63 ± 0.12	$9.66 \pm 1.07 \times 10^{-17}$
2019 Jul. 06	IRDIS $H2$	9.95 ± 0.11	17.54 ± 0.11	$1.24 \pm 0.13 \times 10^{-16}$
	IRDIS $H3$	9.83 ± 0.08	17.41 ± 0.08	$1.18 \pm 0.09 \times 10^{-16}$
2021 Jul. 16	IRDIS $H2$	10.01 ± 0.13	17.60 ± 0.14	$1.17 \pm 0.15 \times 10^{-16}$
	IRDIS $H3$	9.79 ± 0.09	17.37 ± 0.09	$1.23 \pm 0.10 \times 10^{-16}$
2022 May 04	IRDIS $K1$	9.30 ± 0.10	16.87 ± 0.10	$8.49 \pm 0.81 \times 10^{-17}$
	IRDIS $K2$	8.89 ± 0.13	16.45 ± 0.13	$9.65 \pm 1.16 \times 10^{-17}$

correlated with the inclination, which is a common outcome of fitting astrometry that covers a small fraction of the orbit (Ferrer-Chávez et al. 2021). This is also shown in Fig. 5: circular orbits are symmetric with respect to the star, whereas eccentric orbits have a smaller periastron. The orientation of the orbit on the sky is set by the inclination, $i \approx 74$ deg, and the longitude of the ascending node, $\Omega \approx 95$ deg. Since we only fit relative astrometry, there is a second solution for Ω and ω with a difference of $\approx$180 deg.

3.5. Photometric analysis

The contrast measurements and calibrated photometry are listed in Table 4 as magnitudes and fluxes. The dual-band imaging with SPHERE in the $H23$ and $K12$ bands enabled a photometric characterization of the planet, for which we adopted the magnitudes from 2021 and 2022 because these data were obtained with a dedicated strategy for an optimized accuracy of the flux calibration (see Sect. 2.1). Figure 6 shows a color–magnitude diagram that was created with the `species`[8] toolkit (see Stolker et al. 2020 for details). In the figure, HD 135344 Ab is compared with late-type field objects, other directly imaged companions, and synthetic photometry from models. The isochrones that were used to calculate the synthetic fluxes were interpolated from the AMES-Cond and AMES-Dusty grids. These are evolutionary models with a cloudless and a cloudy atmosphere, respectively, as the boundary condition for the interior structure (Chabrier et al. 2000; Allard et al. 2001; Baraffe et al. 2003).

The absolute flux and color of HD 13534 Ab are consistent with the field objects that have a mid-L spectral type. The photospheric temperature of L-type giant planets and brown dwarfs allows for the condensation of refractory species, and their dusty atmospheres therefore cause a red photometric appearance compared to cloudless atmospheres. The atmospheric reddening by clouds is typically stronger for young objects because their surface gravity is lower (e.g., HIP 65426 b; Chauvin et al. 2017). The $H2$–$K1$ color of HD 135344Àb is not unusually red and consistent with the field objects, although it is in particular similar to the reddest objects of that sample. At an age of 12 Myr, the $H2$ luminosity of HD 135344 Ab is consistent with a planetary-mass object of $\approx$10 M_J. We provide a statistical inference of the planetary mass in Sect. 3.7.

3.6. Atmospheric modeling

The spectral appearance and inferred atmospheric parameters provide further insight into the nature of HD 135344 Ab. We compiled the near-infrared SED in Fig. 7 by combining the SPHERE and GRAVITY data. We used the Bayesian framework of the `species` toolkit (Stolker et al. 2020) to fit the data with an atmospheric model, specifically, by interpolating a grid of synthetic spectra from Sonora Diamondback (Morley et al. 2024). This is a radiative-convective equilibrium model that accounts for the condensation of refractory species into cloud particles. The vertical density profile of the cloud deck is parameterized by the sedimentation efficiency, f_sed. The model uses chemical

[8] https://github.com/tomasstolker/species

Table 5. Planet parameters of HD 135344 Ab.

Parameter	Value	Units
Orbit fit		
a	$16.5^{+2.8}_{-2.0}$	au
e	$0.5^{+0.2}_{-0.2}$	
i	$73.6^{+2.8}_{-4.7}$	deg
Ω^a	$94.9^{+1.8}_{-3.1}$	deg
ω^b	$8.2^{+8.7}_{-10.8}$	deg
t_p	65405^{+2026}_{-1378}	MJD
Atmosphere fit		
T_eff	1510^{+35}_{-35}	K
$\log g$	$4.14^{+0.06}_{-0.07}$	dex
[M/H]	$\gtrsim$0.0	dex
f_sed	$\lesssim$1.5	
R_p	$1.60^{+0.07}_{-0.06}$	R_J
A_V	$\lesssim$0.5	mag
Evolution fit^c		
Age	12^{+3}_{-4}	Myr
M_p	$10.0^{+1.4}_{-1.9}$	M_J
T_eff	1585^{+82}_{-73}	K
$\log g$	$4.1^{+0.1}_{-0.1}$	dex
R_p	$1.45^{+0.06}_{-0.03}$	R_J

Notes. The listed values are the median and the 16th and 84th percentiles from the posterior distributions. We only accounted for the statistical uncertainties. The lower and upper limits are provided as the 16th and 84th percentile, respectively. $^{(a,b)}$The table includes one solution for ω and Ω, but there is a second solution with an offset of 180 deg. $^{(c)}$The age and planet mass were free parameters, whereas T_eff, R_p, and $\log g$ were interpolated from the evolutionary grid based on the posterior samples.

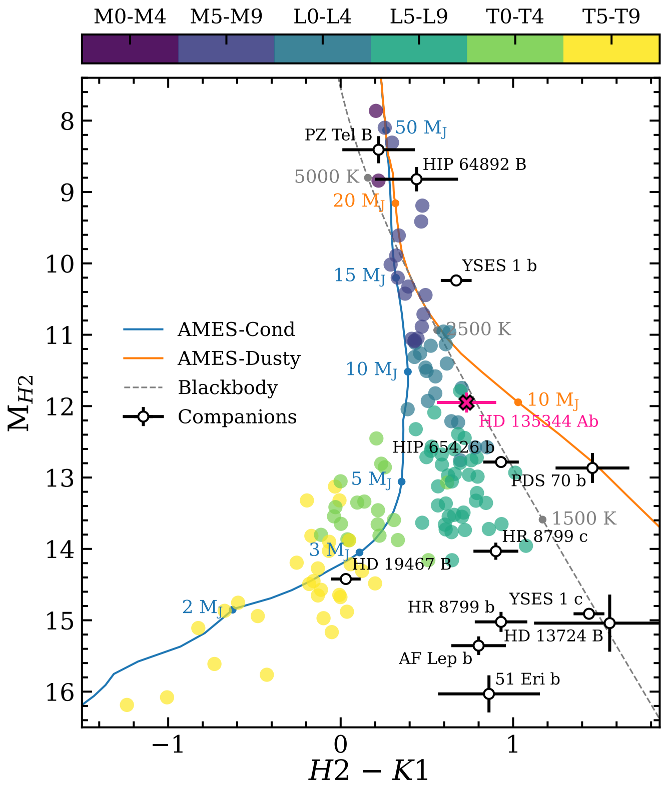

Fig. 6. Color–magnitude diagram of M_{H2} vs. $H2 - K1$. The field objects are color-coded by M, L, and T spectral types, and the directly imaged companions are labeled individually. HD 135344 Ab is highlighted with a pink cross. The blue and orange lines show the synthetic colors computed from the AMES-Cond and AMES-Dusty evolutionary tracks at an age of 12 Myr. Blackbody emission is shown for an object with a radius of 1 R_J (dashed gray line).

equilibrium, which is a reasonable assumption in the temperature regime of HD 135344 Ab, where CO will be the dominant carbon-bearing species. The parameters were estimated with the nested sampling algorithm from `MultiNest` (Feroz & Hobson 2008; Buchner et al. 2014), using 2000 live points and accounting for the spectral covariances.

The photometry and spectra are compared with the best-fit model spectrum in Fig. 7, which has a goodness-of-fit statistic of $\chi^2_\nu = 1.3$. The IFS spectra have a low S/N (see Sect. 2.1), but the broad H_2O absorption feature between the J and H bands is visible in the YJH spectrum. The GRAVITY spectrum also shows slopes in the pseudo-continuum that are expected to be caused by H_2O opacities. The CO bandheads might tentatively be detected in the K band, but the GRAVITY spectrum also shows correlated noise that appears with a frequency and amplitude that might mimic the CO bands. The initial residuals indeed showed that the systematics were not fully accounted for by the covariances, and we therefore fit an uncertainty inflation for the GRAVITY spectrum. This yielded a 10 ± 2% increase relative to the model fluxes. From the photometry, the $H3$ flux of the first epoch is in particular discrepant with the best-fit model, possibly due to the poorer observing conditions and because continuous satellite spots for the calibration were lacking (see Sect. 2.1).

The inferred parameters are listed in Table 5. The temperature, $T_\mathrm{eff} \approx 1510$ K, is consistent with a mid L-type object, as empirically estimated from the $H2$ brightness in Fig. 6. The surface gravity, log g, and metallicity, [M/H], are challenging to constrain from the low-resolution spectra because this requires a highly accurate calibration, while the parameters might easily be biased otherwise. We therefore adopted the constraint from the evolution fit, log $g = 4.1 \pm 0.1$ (see Sect. 3.7), as the normal prior for the atmospheric fit. The likelihood of the metallicity peaked at the supersolar edge of the model grid, but the data are also consistent with the solar abundances. The low sedimentation parameter clearly favors a dusty atmosphere, while we can rule out an atmosphere with strongly settled clouds. When we repeated the fit with a fixed sedimentation parameter of $f_\mathrm{sed} = 8$, this resulted in a Bayes factor of $\Delta \ln \mathcal{Z} = 43$ relative to the model in which f_sed was a free parameter.

From the T_eff and R_p posterior posterior, we computed the bolometric luminosity, $\log L/L_\odot = -3.9 \pm 0.1$. We note that the statistical uncertainty on the luminosity was only ≈0.01 dex, and we therefore reran the spectral fit using five other cloudy models: Exo-REM (Charnay et al. 2018), petitCODE (Mollière et al. 2015), DRIFT-PHOENIX (Helling et al. 2008), BT-Settl (Allard et al. 2012), and AMES-Dusty (Allard et al. 2001). The dispersion on the retrieved luminosity, $\Delta \log L/L_\odot \approx 0.1$ dex, was adopted as the approximate systematic uncertainty. In the next section, we use the luminosity to quantify the mass of the planet.

3.7. Bulk parameters and evolutionary constraints

In Sect. 3.5 we showed that the H-band luminosity of HD 135344 Ab is consistent with a dusty mid L-type object with an approximate mass of 10 M_J. We now quantify the mass and other bulk parameters using the `species` toolkit. To do this, we fit the bolometric luminosity, $\log L/L_\odot = -3.9 \pm 0.1$, which we inferred from the atmospheric modeling, with a grid of evolutionary tracks that we interpolated as function of mass and age. The age of the system was applied as asymmetric normal prior by adopting the pre-main-sequence age of HD 135344 B, $11.9^{+3.7}_{-5.8}$ Myr (Garufi et al. 2018). Similar to the spectral fit, a main limitation here are non-linear variations in the model grid, which can lead to inaccuracies and underestimated uncertainties. For the fit, we used the ATMO model (Phillips et al. 2020) because the cooling tracks seemed to be reasonably spaced for interpolation. The parameters were estimated with `MultiNest` (Feroz & Hobson 2008; Buchner et al. 2014) by sampling the posterior distributions with 1000 live points.

The mass and evolutionary constraints are presented in Fig. 8, which shows the isochrones and cooling tracks that describe the luminosity and age of HD 135344 Ab. We inferred a mass of $M_\mathrm{p} \approx 10\ M_\mathrm{J}$, and the age is consistent with the prior, but is slightly more constrained (see Table 5). After the fit, we interpolated the evolutionary grid again for each mass-age sample in order to extract the related temperature, $T_\mathrm{eff} \approx 1585$, surface gravity, $\log g \approx 4.1$, and radius, $R_\mathrm{p} \approx 1.5$. Table 5 shows that the inferred bulk parameters are consistent within the considered credible regions with the parameter values estimated with the spectral modeling in Sect. 3.6. This suggests that the results are robust because we used two different, although correlated, approaches. The exception is the radius, which differs by 2σ between the atmospheric and the evolution fit.

4. Discussion and conclusions

We have reported the direct discovery of a young giant planet at the A0V-type star HD 135344 A. The planet was detected through high-contrast imaging and interferometric observations. Our astrometric analysis of seven datasets, with a total baseline of four years, showed that the object is comoving with the

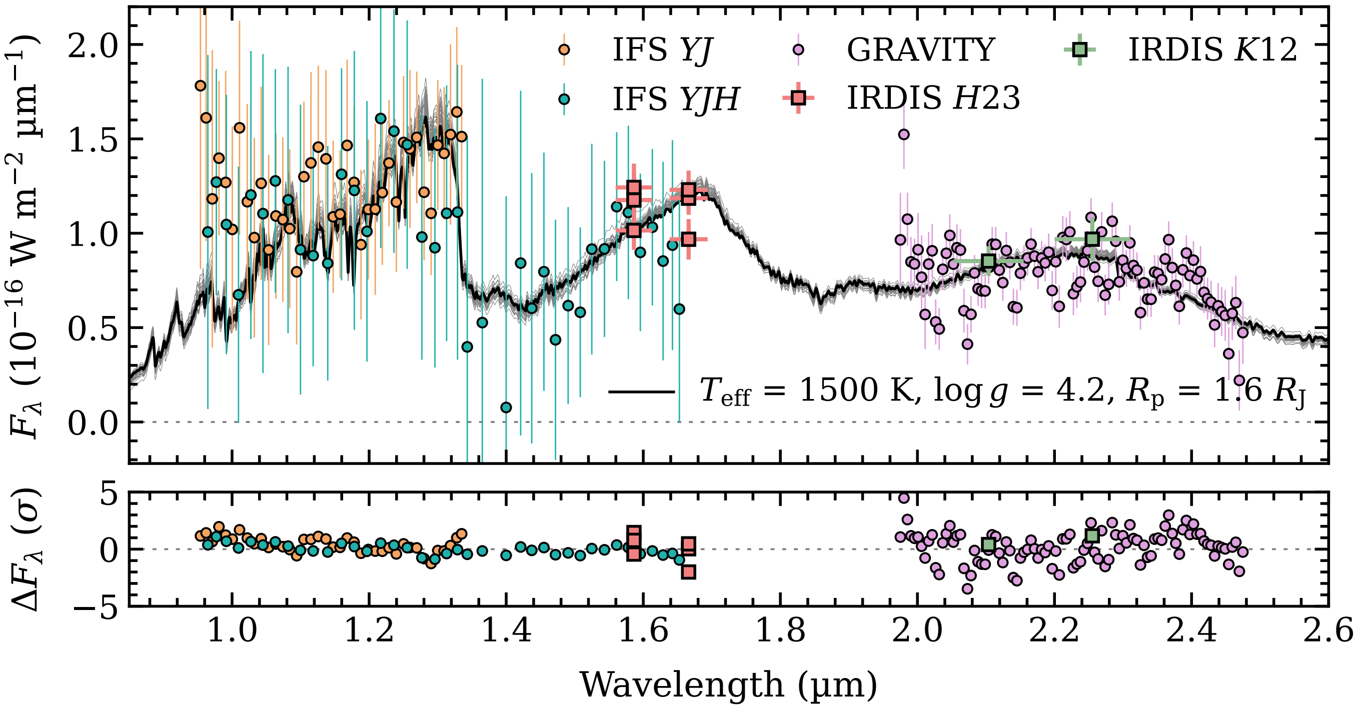

Fig. 7. Near-infrared spectral energy distribution of HD 135344 Ab. The black line shows the best-fit model spectrum from Sonora Diamondback, and the gray lines show 30 random samples from the posterior distribution, both shown at R = 500. The SPHERE/IFS and GRAVITY spectra are shown with circular markers, and the latter are downsampled for clarity. The SPHERE/IRDIS photometry is shown by square markers, with horizontal error bars indicating the FWHM of the corresponding filter profiles. The bottom panel shows the residuals of the best-fit model, calculated at the resolution and wavelength sampling of the data.

central star. This was confirmed both by a common parallax and common proper motion. The inferred atmospheric and bulk parameters indicate a planetary nature, with a model-dependent mass of $M_{\rm p} \approx 10\ M_{\rm J}$. The planet position changed by ≈30 mas and is slightly curved, which yielded a constraint on the orbital semi-major axis of approximately 15–20 au.

When we adopt the pre-main-sequence age of ≈12 Myr from the secondary star, HD 135344 Ab might be the youngest directly imaged planet that has fully formed and orbits on Solar System scales. Figure 9 shows a comparison with the ages and semi-major axes of other close-in directly imaged planets. Young directly imaged planets at small separations (≲100 au) have only been detected at intermediate-mass stars. The planets in Fig. 9 all orbit A- and F-type stars, and the discovery of HD 135344 Ab at an A0-type star therefore follows that trend. This contrasts young planetary-mass objects on wide orbits (≳100 au), which are typically found at late-type stars (e.g., Bowler et al. 2014). Because the orbit of HD 135344 Ab is relatively small, this planetary-mass companion is expected to have formed in a protoplanetary disk and is likely not the low-mass tail of binary star formation. The current planet location might be in the vicinity of the approximate snowline location for the spectral type of the host star (see Fig. 9), although the planet may have migrated during its formation phase.

In addition to the age constraint from HD 135344 B, Ratzenböck et al. (2023) recently used a clustering algorithm to map the star formation history of Sco-Cen. HD 135344 AB was associated with the ϕ Lup group in UCL, for which an isochrone age of ≈10 and ≈17 Myr was determined with two evolutionary models. An age of 10 Myr would match the pre-main-sequence age of HD 135344 B. Arguably, it is also be more consistent with the high IR excess of the secondary star, because it would be (even more) puzzling if a dust-rich disk were maintained up to 17 Myr. If the system were to be ≈17 Myr old, then the planet mass would still be in the planetary regime, $M_{\rm p} \approx 12\ M_{\rm J}$, but close to the deuterium-burning limit.

In contrast to the secondary star, the circumstellar environment of HD 135344 A is already depleted, given the minor IR excess (see Appendix A). This is also consistent with a non-detection of a disk in scattered light in the SPHERE imagery. The origin of the different disk evolution timescales of the primary and secondary star is not known, but it might be related to a more efficient photoevaporation by the stronger radiation field of HD 135344 A. Disk lifetimes are indeed known to increase toward later spectral types (e.g., Luhman 2022). During the early evolution of the system, the primary star likely was a Herbig Ae star with a protoplanetary disk in which HD 135344 Ab would have carved a wide gap during its formation. Dust- and gas-depleted cavities and gaps are quite common at Herbig Ae stars (e.g., van der Marel & Mulders 2021). These resolved substructures are signposts for forming planets, but only a few gap-carving planets have been detected (e.g., PDS 70 b/c; Keppler et al. 2018; Haffert et al. 2019). The discovery of close-in directly imaged planets such as HD 135344 Ab shows that Jovian planets might indeed have caused at least some of the large cavities. They might be more difficult to detect during formation because the dust has not yet been dispersed because even cavities are not fully cleared from small dust.

HD 135344 Ab is an appealing target for a spectral characterization with the next generation of large ground-based telescope facilities (e.g., Brandl et al. 2010) because of its small angular and physical separation from the star. The quality of the current measurements was sufficient to identify H_2O absorption in the low-resolution spectra and to infer the bulk parameters.

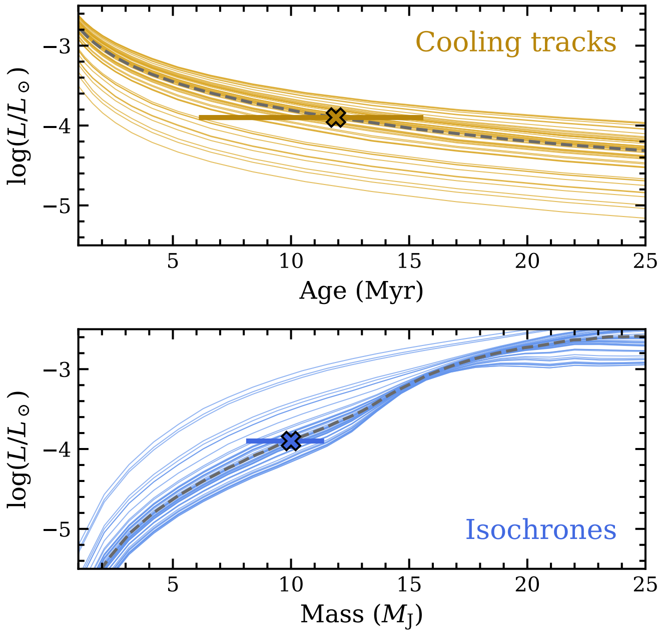

Fig. 8. Cooling tracks and isochrones inferred from the planetary luminosity. The colored lines show 50 random samples from the posterior distributions. The best-fit model is shown with the dashed line in each panel. The crosses represent the luminosity of HD 135344 Ab, $\log L/L_{\odot} = -3.9 \pm 0.1$, and the horizontal error bars indicate the prior age and posterior mass in the top and bottom panel, respectively.

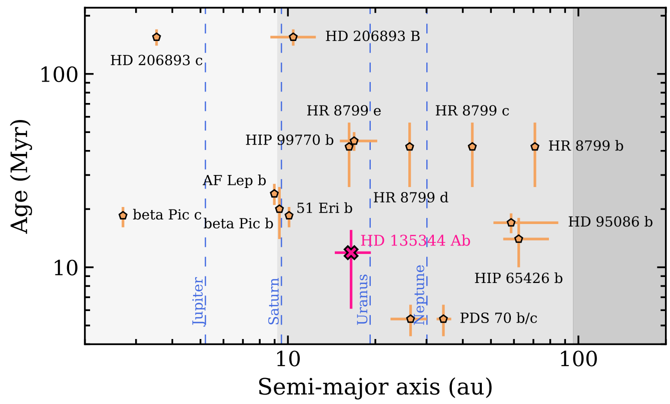

Fig. 9. Age vs. semi-major axis of directly imaged planets. We selected young companions with planetary masses (except for HD 206893 B), $M \lesssim 13\ M_{\rm J}$, planet-to-star mass ratios of $q \lesssim \frac{1}{25}$, and orbits smaller than ≈100 au. The locations of the giant planets in the Solar System are indicated with vertically dashed lines, and the gray areas from left to right are separated by the approximate locations of the H_2O and CO_2 ice lines of an A0-type star (Öberg et al. 2011). The semi-major axes were retrieved from `whereistheplanet` when available (Wang et al. 2021a), and from Wang et al. (2021b), Hinkley et al. (2023), Currie et al. (2023), and De Rosa et al. (2023) otherwise. The ages were adopted from Pecaut et al. (2012), Bell et al. (2015), Macintosh et al. (2015), Chauvin et al. (2017), Müller et al. (2018), Garufi et al. (2018), Zuckerman (2019), Miret-Roig et al. (2020), Brandt et al. (2021), and Hinkley et al. (2023). Systematic uncertainties on the ages (e.g., due to uncertain cluster membership) are not reflected by the error bars.

A spectral inference of the molecular abundances will be more challenging because the planet is faint, but it might be feasible with KPIC, the fiber-fed high-resolution infrared spectrograph at Keck (Wang et al. 2024), or with the enhanced sensitivity of the recent upgrade to GRAVITY+ (GRAVITY+ Collaboration 2022). Extending the SED from NIR to MIR wavelengths will increase the accuracy on the bolometric luminosity and other bulk parameters, and so will the extraction and calibration at short NIR wavelengths. Specifically, the fluxes at the blue end ($\lambda \lesssim 1.1$ μm) of the IFS spectrum are systematically higher than the model spectra in Fig. 7. We suspect that this is a bias in the spectral extraction, possibly due to the lower planet contrast, enhanced speckle noise, and/or reduced instrument transmission at the shortest wavelengths. Similar contaminating systematics are also seen at the short wavelengths in the IFS spectra of other faint planets (e.g. Samland et al. 2017). The effect did not impact the parameter estimation given the S/N of the spectra. Since the inferred luminosity is consistent with a planet mass of $M_{\rm p} \approx 10\ M_{\rm J}$, but the $R_{\rm p}$ from the spectral fit is slightly too large given the mass and age constraint, this might imply that the $T_{\rm eff}$ and $R_{\rm p}$ inferred from the SED are somewhat under- and overestimated, respectively.

The orbital analysis yielded first constraints on the elements, given that the astrometry covers about 9% of the orbital period, $P \approx 45$ yr. The semi-major axis has a precision of ≈2–3 au, but is correlated with the poorly constrained eccentricity, and therefore, also with the inclination. The posterior favors low to intermediate eccentricities, ruling out highly eccentric face-on orbits. However, this result requires confirmation through continued astrometric monitoring. The projected motion will be somewhat linear during the coming years, while the curvature will again increase toward periastron, which is in 2038.5 ± 4.4. Since the planet orbit has an high inclination, we conclude that the orbit is not coplanar with the protoplanetary disk of the secondary star in the HD 135344 AB binary system, as it is seen close to face-on ($i_{\rm disk} \approx 20$ deg; e.g. Pérez et al. 2014). This is also not surprising, given the large projected separation between the two stars (≈2800 au); their circumstellar environments are therefore expected to have evolved independently.

Since the star was not observed by Hipparcos, we are unable to determine a proper motion anomaly. It will be interesting to analyze the astrometric measurements from *Gaia* DR4. Although the orbital period of HD 135344 Ab is ≈45 years and the baseline of DR4 is 5.5 years, an acceleration of the stellar proper motion might be detectable. When future *Gaia* epoch astrometry will be included in the orbit fit, a first constraint on the dynamical mass can be obtained, which will be valuable given the early evolutionary stage of the planet and its possible formation in a protoplanetary disk. Furthermore, a combined analysis of the absolute and relative astrometry could place constraints on the multiplicity of the planetary system because close-in directly imaged planets are often found in pairs (e.g., at β Pic, HD 206893, and PDS 70).

The detection of HD 135344 Ab at only 3–4λ/D demonstrates the powerful high-contrast and high-resolution capabilities of the SPHERE and GRAVITY instrument. This study also highlights the importance of high-precision astrometric measurements to fully disentangle orbital from background motion in a region of non-stationary background stars. A good portion of luck was involved with the discovery of HD 135344 Ab, however, because we caught the planet at a favorable separation along its inclined orbit. In the next 10 to 20 years, the angular separation with its star will decrease to ≈10–35 mas, which means that the planet would not have been discovered with SPHERE for a large fraction of its orbit.

Finally, direct imaging surveys have established that giant planets are rare at separations ≳20 au (Nielsen et al. 2019;

Vigan et al. 2021). The detection rate is expected to increase toward shorter separations, where radial velocity surveys have revealed a turnover point in the occurrence rates (Fernandes et al. 2019; Fulton et al. 2021). *Gaia* DR4 may reveal hints of similar close-in giant planets in star-forming regions, which will guide direct imaging searches and post-processing algorithms (e.g., Currie et al. 2023; Winterhalder et al. 2024). HD 135344 Ab might be part of a population of giant planets that could have formed in the vicinity of the snowline. These objects have remained challenging to detect since most surveys and observing strategies have not been optimized for such small separations.

Acknowledgements. We thank the referee for the helpful and constructive feedback. Based on observations collected at the European Southern Observatory under ESO programmes 0103.C-0189(A), 105.20A8.001, 109.22ZA.004, 1104.C-0651(G), and 111.24FS.001. T.S. acknowledges the support from the Netherlands Organisation for Scientific Research (NWO) through grant VI.Veni.202.230. J.J.W. is supported by NASA XRP Grant 80NSSC23K0280. S.L. acknowledges the support of the French Agence Nationale de la Recherche (ANR), under grant ANR-21-CE31-0017 (project ExoVLTI). Part of this work was performed using the ALICE compute resources provided by Leiden University. This work used the Dutch national e-infrastructure with the support of the SURF Cooperative using grant no. EINF-1620. This research has made use of the Jean-Marie Mariotti Center `Aspro` service.

References

Allard, F., Hauschildt, P. H., Alexander, D. R., Tamanai, A., & Schweitzer, A. 2001, ApJ, 556, 357
Allard, F., Homeier, D., & Freytag, B. 2012, Phil. Trans. R. Soc. London Ser. A, 370, 2765
Amara, A., & Quanz, S. P. 2012, MNRAS, 427, 948
Balmer, W. O., Otten, G. P. P. L., & Stolker, T. 2025, `https://doi.org/10.5281/zenodo.14838369`
Baraffe, I., Chabrier, G., Barman, T. S., Allard, F., & Hauschildt, P. H. 2003, A&A, 402, 701
Bell, C. P. M., Mamajek, E. E., & Naylor, T. 2015, MNRAS, 454, 593
Beuzit, J. L., Vigan, A., Mouillet, D., et al. 2019, A&A, 631, A155
Blunt, S., Wang, J. J., Angelo, I., et al. 2020, AJ, 159, 89
Bohlin, R. C., Gordon, K. D., & Tremblay, P. E. 2014, PASP, 126, 711
Bowler, B. P., Liu, M. C., Kraus, A. L., & Mann, A. W. 2014, ApJ, 784, 65
Brandl, B. R., Lenzen, R., Pantin, E., et al. 2010, SPIE Conf. Ser., 7735, 77352G
Brandt, G. M., Brandt, T. D., Dupuy, T. J., Michalik, D., & Marleau, G.-D. 2021, ApJ, 915, L16
Brown, J. M., Blake, G. A., Qi, C., et al. 2009, ApJ, 704, 496
Buchner, J., Georgakakis, A., Nandra, K., et al. 2014, A&A, 564, A125
Chabrier, G., Baraffe, I., Allard, F., & Hauschildt, P. 2000, ApJ, 542, 464
Charnay, B., Bézard, B., Baudino, J. L., et al. 2018, ApJ, 854, 172
Chauvin, G., Desidera, S., Lagrange, A. M., et al. 2017, A&A, 605, L9
Claudi, R. U., Turatto, M., Gratton, R. G., et al. 2008, SPIE Conf. Ser., 7014, 70143E
Coulson, I. M., & Walther, D. M. 1995, MNRAS, 274, 977
Cugno, G., Leisenring, J., Wagner, K. R., et al. 2024, AJ, 167, 182
Currie, T., Brandt, G. M., Brandt, T. D., et al. 2023, Science, 380, 198
Cutri, R. M., Skrutskie, M. F., van Dyk, S., et al. 2003, 2MASS All Sky Catalog of point sources
De Rosa, R. J., Nielsen, E. L., Wahhaj, Z., et al. 2023, A&A, 672, A94
Dohlen, K., Langlois, M., Saisse, M., et al. 2008, SPIE Conf. Ser., 7014, 70143L
Fairlamb, J. R., Oudmaijer, R. D., Mendigutía, I., Ilee, J. D., & van den Ancker, M. E. 2015, MNRAS, 453, 976
Fernandes, R. B., Mulders, G. D., Pascucci, I., Mordasini, C., & Emsenhuber, A. 2019, ApJ, 874, 81
Feroz, F., & Hobson, M. P. 2008, MNRAS, 384, 449
Ferrer-Chávez, R., Wang, J. J., & Blunt, S. 2021, AJ, 161, 241
Fulton, B. J., Rosenthal, L. J., Hirsch, L. A., et al. 2021, ApJS, 255, 14
Gaia Collaboration (Vallenari, A., et al.) 2023, A&A, 674, A1
Garufi, A., Quanz, S. P., Avenhaus, H., et al. 2013, A&A, 560, A105
Garufi, A., Benisty, M., Pinilla, P., et al. 2018, A&A, 620, A94
GRAVITY Collaboration (Abuter, R., et al.) 2017, A&A, 602, A94
GRAVITY Collaboration (Lacour, S., et al.) 2019, A&A, 623, L11
GRAVITY Collaboration (Nowak, M., et al.) 2020, A&A, 633, A110
GRAVITY+ Collaboration (Abuter, R., et al.) 2022, The Messenger, 189, 17
Haffert, S. Y., Bohn, A. J., de Boer, J., et al. 2019, Nat. Astron., 3, 749
Helling, C., Dehn, M., Woitke, P., & Hauschildt, P. H. 2008, ApJ, 675, L105
Hinkley, S., Lacour, S., Marleau, G. D., et al. 2023, A&A, 671, L5
Høg, E., Fabricius, C., Makarov, V. V., et al. 2000, A&A, 355, L27
Houk, N. 1982, Michigan Catalogue of Two-dimensional Spectral Types for the HD stars. Volume_3. Declinations -40_f0 to -26_f0 (Ann Arbor: University of Michigan)
Keppler, M., Benisty, M., Müller, A., et al. 2018, A&A, 617, A44
Lacour, S., Wang, J. J., Nowak, M., et al. 2020, SPIE Conf. Ser., 11446, 114460O
Luhman, K. L. 2022, AJ, 163, 25
Macintosh, B., Graham, J. R., Barman, T., et al. 2015, Science, 350, 64
Maire, A. L., Stolker, T., Messina, S., et al. 2017, A&A, 601, A134
Mason, B. D., Wycoff, G. L., Hartkopf, W. I., Douglass, G. G., & Worley, C. E. 2001, AJ, 122, 3466
Miret-Roig, N., Galli, P. A. B., Brandner, W., et al. 2020, A&A, 642, A179
Mollière, P., van Boekel, R., Dullemond, C., Henning, T., & Mordasini, C. 2015, ApJ, 813, 47
Morley, C. V., Mukherjee, S., Marley, M. S., et al. 2024, ApJ, 975, 59
Müller, A., Keppler, M., Henning, T., et al. 2018, A&A, 617, L2
Muto, T., Grady, C. A., Hashimoto, J., et al. 2012, ApJ, 748, L22
Nielsen, E. L., Rosa, R. J. D., Rameau, J., et al. 2017, AJ, 154, 218
Nielsen, E. L., De Rosa, R. J., Macintosh, B., et al. 2019, AJ, 158, 13
Nowak, M., Lacour, S., Lagrange, A. M., et al. 2020, A&A, 642, L2
Öberg, K. I., Murray-Clay, R., & Bergin, E. A. 2011, ApJ, 743, L16
Pecaut, M. J., Mamajek, E. E., & Bubar, E. J. 2012, ApJ, 746, 154
Pérez, L. M., Isella, A., Carpenter, J. M., & Chandler, C. J. 2014, ApJ, 783, L13
Phillips, M. W., Tremblin, P., Baraffe, I., et al. 2020, A&A, 637, A38
Ratzenböck, S., Großschedl, J. E., Alves, J., et al. 2023, A&A, 678, A71
Samland, M., Mollière, P., Bonnefoy, M., et al. 2017, A&A, 603, A57
Samland, M., Bouwman, J., Hogg, D. W., et al. 2021, A&A, 646, A24
Siess, L., Dufour, E., & Forestini, M. 2000, A&A, 358, 593
Speagle, J. S. 2020, MNRAS, 493, 3132
Stolker, T., Sitko, M., Lazareff, B., et al. 2017, ApJ, 849, 143
Stolker, T., Bonse, M. J., Quanz, S. P., et al. 2019, A&A, 621, A59
Stolker, T., Quanz, S. P., Todorov, K. O., et al. 2020, A&A, 635, A182
van der Marel, N., & Mulders, G. D. 2021, AJ, 162, 28
Vigan, A. 2020, Astrophysics Source Code Library [`record ascl:2009.002`]
Vigan, A., Moutou, C., Langlois, M., et al. 2010, MNRAS, 407, 71
Vigan, A., Fontanive, C., Meyer, M., et al. 2021, A&A, 651, A72
Wang, J. J., Kulikauskas, M., & Blunt, S. 2021a, Astrophysics Source Code Library [`record ascl:2101.003`]
Wang, J. J., Vigan, A., Lacour, S., et al. 2021b, AJ, 161, 148
Wang, J. J., Mawet, D., Xuan, J. W., et al. 2024, SPIE Conf. Ser., 13096, 130961X
Widmann, F., Gillessen, S., Ott, T., et al. 2022, SPIE Conf. Ser., 12183, 121830U
Winterhalder, T. O., Lacour, S., Mérand, A., et al. 2024, A&A, 688, A44
Wright, E. L., Eisenhardt, P. R. M., Mainzer, A. K., et al. 2010, AJ, 140, 1868
Zuckerman, B. 2019, ApJ, 870, 27

[1] Leiden Observatory, Leiden University, Einsteinweg 55, 2333 CC Leiden, The Netherlands
[2] Max Planck Institute for Astronomy, Königstuhl 17, 69117 Heidelberg, Germany
[3] Department of Astrophysics/IMAPP, Radboud University, Heyendaalseweg 135, 6525 AJ Nijmegen, The Netherlands
[4] European Southern Observatory, Karl-Schwarzschild-Straße 2, 85748 Garching, Germany
[5] Department of Physics & Astronomy, Johns Hopkins University, 3400 N. Charles Street, Baltimore, MD 21218, USA
[6] Space Telescope Science Institute, 3700 San Martin Drive, Baltimore, MD 21218, USA
[7] LESIA, Observatoire de Paris, PSL, CNRS, Sorbonne Université, Université de Paris, 5 place Janssen, 92195 Meudon, France
[8] Department of Astrophysical & Planetary Sciences, JILA, Duane Physics Bldg., 2000 Colorado Ave, University of Colorado, Boulder, CO 80309, USA
[9] Center for Interdisciplinary Exploration and Research in Astrophysics (CIERA) and Department of Physics and Astronomy, Northwestern University, Evanston, IL 60208, USA
[10] Institute of Astronomy, University of Cambridge, Madingley Road, Cambridge CB3 0HA, UK
[11] Univ. Grenoble Alpes, CNRS, IPAG, 38000 Grenoble, France
[12] Academia Sinica, Institute of Astronomy and Astrophysics, 11F Astronomy-Mathematics Building, NTU/AS campus, No. 1, Section 4, Roosevelt Rd., Taipei 10617, Taiwan

[13] Anton Pannekoek Institute for Astronomy, University of Amsterdam, Science Park 904, 1098 XH Amsterdam, The Netherlands
[14] SRON Netherlands Institute for Space Research, Sorbonnelaan 2, 3584 CA Utrecht, The Netherlands
[15] Institute for Particle Physics and Astrophysics, ETH Zurich, Wolfgang-Pauli-Strasse 27, 8093 Zurich, Switzerland
[16] Universidade de Lisboa - Faculdade de Ciências, Campo Grande, 1749-016 Lisboa, Portugal
[17] CENTRA - Centro de Astrofísica e Gravitação, IST, Universidade de Lisboa, 1049-001 Lisboa, Portugal
[18] Max Planck Institute for extraterrestrial Physics, Giessenbachstraße 1, 85748 Garching, Germany
[19] Université Côte d'Azur, Observatoire de la Côte d'Azur, CNRS, Laboratoire Lagrange, Bd de l'Observatoire, CS 34229, 06304 Nice Cedex 4, France
[20] Aix Marseille Univ, CNRS, CNES, LAM, Marseille, France
[21] STAR Institute, Université de Liège, Allée du Six Août 19c, 4000 Liège, Belgium
[22] Institute of Physics, University of Cologne, Zülpicher Straße 77, 50937 Cologne, Germany
[23] Max Planck Institute for Radio Astronomy, Auf dem Hügel 69, 53121 Bonn, Germany
[24] Universidade do Porto, Faculdade de Engenharia, Rua Dr. Roberto Frias, 4200-465 Porto, Portugal
[25] School of Physics, University College Dublin, Belfield, Dublin 4, Ireland
[26] Astrophysics Group, Department of Physics & Astronomy, University of Exeter, Stocker Road, Exeter, EX4 4QL, UK
[27] Departments of Physics and Astronomy, Le Conte Hall, University of California, Berkeley, CA 94720, USA
[28] European Southern Observatory, Casilla 19001, Santiago 19, Chile
[29] Advanced Concepts Team, European Space Agency, TEC-SF, ESTEC, Keplerlaan 1, NL-2201, AZ Noordwijk, The Netherlands
[30] University of Exeter, Physics Building, Stocker Road, Exeter EX4 4QL, UK
[31] Fakultät für Physik, Universität Duisburg-Essen, Lotharstraße 1, 47057 Duisburg, Germany
[32] Institüt für Astronomie und Astrophysik, Universität Tübingen, Auf der Morgenstelle 10, 72076 Tübingen, Germany
[33] Astronomy Department, University of Michigan, Ann Arbor, MI 48109 USA
[34] European Space Agency (ESA), ESA Office, Space Telescope Science Institute, 3700 San Martin Drive, Baltimore, MD 21218, USA
[35] Department of Earth & Planetary Sciences, Johns Hopkins University, Baltimore, MD, USA
[36] Max Planck Institute for Astrophysics, Karl-Schwarzschild-Str. 1, 85741 Garching, Germany
[37] Excellence Cluster ORIGINS, Boltzmannstraße 2, 85748 Garching bei München, Germany
[38] The Kavli Institute for Astronomy and Astrophysics, Peking University, Beijing 100871, PR China

Appendix A: Stellar parameters

In this appendix, we analyze the spectral energy distribution (SED) of HD 135344 A. This is important for the calibration of the contrast measurements and, given the age of the system, to identify potential IR excess by circumstellar dust. Similar to fit of the near-infrared planet SED in Sect. 3.6, we used `species` (Stolker et al. 2020) to model the stellar SED and retrieve the atmospheric parameters, in this case using the BT-NextGen model spectra (Allard et al. 2012). The parameter posteriors were then used for computing synthetic photometry and spectra of the star, in order to convert the contrast to flux. The main stellar parameters are listed in Table A.

The parameter estimation is based on the low-resolution Gaia XP spectrum, and Gaia G and G_{RVS}, TYCHO BV, and 2MASS JHK_{s} photometry. We fitted an error bar inflation for the XP spectrum to account for the systematics that were seen as low-frequency oscillations. Similarly, we inflated the uncertainty of the G_{RVS} flux. The best-fit model spectrum has a goodness-of-fit of $\chi^2_\nu = 0.94$ and is compared with the data in Fig. A.1. The WISE fluxes were not included in the fit since the residuals revealed excess emission starting at WISE $W3$ ($\lambda_0 \approx 12\ \mu$m) or perhaps already at $W2$ ($\lambda_0 \approx 4.6\ \mu$m). The WISE photometry is however flagged as possibly contaminated by a diffraction spike of the secondary star, which has a high IR excess. Also, the initial WISE magnitudes are ≈0.2 and ≈2.0 mag fainter in $W3$ and $W4$, respectively, compared to the ALLWISE release (Wright et al. 2010). Extracting robust photometry might be difficult since the two stars are hardly resolved at $W4$. So, while there seems to be evidence for IR excess, the magnitude is yet to determined. A more detailed analysis of the potential circumstellar disk will be deferred to a followup work.

The retrieved stellar parameters are provided in Table A. The error bars reflect only the statistical uncertainties from the Bayesian inference, which might be be underestimated because model-dependent systematics are not accounted for. The effective temperature, $T_{\mathrm{eff}} \approx 9540$ K, is consistent with an A0V type star as evolutionary tracks predict about 9500 K for a stellar mass of $M_* = 2.2\ M_\odot$ (see Fig. A.2). The posterior distribution of the metallicity peaks near zero, the lower boundary of the model grid, indicating a preference for solar abundances. The visual extinction, $A_V \approx 0.2$, is consistent with the value derived for HD 135344 B, $A_V = 0.23 \pm 0.06$, by Fairlamb et al. (2015). The radius, $R_* \approx 1.5\ R_\odot$, is smaller than the model prediction, $R_* = 1.8\ R_\odot$. The radius acts as a flux scaling of the model spectrum, together with the normal prior for the parallax. The Gaia astrometric solution has a RUWE of 0.95 and the astrometric excess noise is 0.21 mas, indicating that the parallax measurement is sufficiently reliable to not bias the inferred stellar radius. From T_{eff} and R_*, we computed a bolometric luminosity of $\log L_*/L_\odot = 1.22 \pm 0.01$. The luminosity is low for an A0V type star (see Fig. A.2), as a result of the small inferred stellar radius.

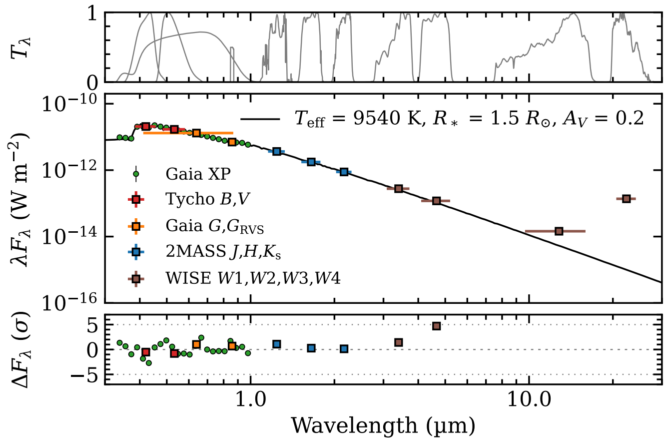

Fig. A.1: Spectral energy distribution of HD 135344 A. The black line is the best-fit model spectrum and the colored markers are the photometric fluxes with horizontal error bars showing the FWHM of the filters. The top panel shows the filter profiles and the bottom panel the residuals relative to the measurement uncertainties. For clarity, every 15th wavelength of the Gaia XP spectrum is shown, whereas the full spectrum was used in the fit.

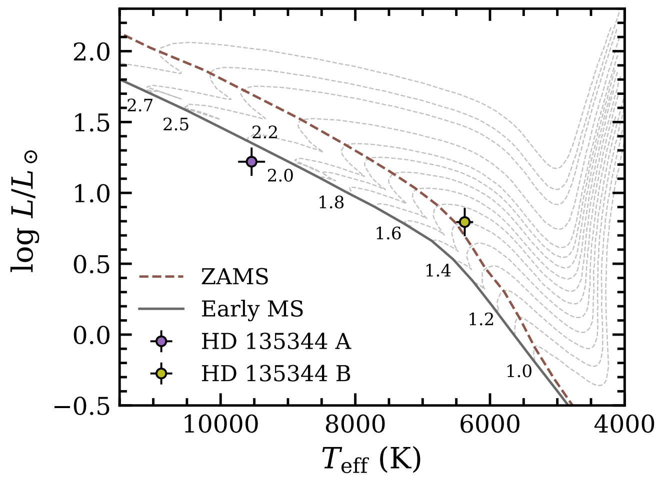

Fig. A.2: Stellar evolutionary tracks in comparison with the HD 135344 AB binary system. The parameters of the primary star have been estimated in this work, but here showing inflated uncertainties of $\sigma_{T_{\mathrm{eff}}} = 200$ K and $\sigma_{\log L/L_\odot} = 0.1$ dex. The parameters of the secondary star have been adopted from Fairlamb et al. (2015) and were corrected to the Gaia DR3 distance. The pre-main-sequence tracks are adopted from Siess et al. (2000). Stellar masses are provided next to the pre-main-sequence tracks in solar masses. The brown dashed line shows the zero age main-sequence (ZAMS; $L_{\mathrm{nuclear}} > 0.99 L_{\mathrm{total}}$), which is at 13.7 Myr for HD 135344 B ($M_* = 1.5\ M_\odot$). The solid line is the early main-sequence, defined as the moment when the CNO cycle of intermediate-mass stars has reached its equilibrium.

Table A.1: Stellar parameters of HD 135344 A.

Parameter	Value	Units	Reference
RA (J2016)	+15 15 48.92	hms	Gaia Collaboration (2023)
Dec (J2016)	-37 08 56.12	dms	Gaia Collaboration (2023)
μ_{RA}	-18.74 ± 0.05	mas yr^{-1}	Gaia Collaboration (2023)
μ_{Dec}	-24.01 ± 0.04	mas yr^{-1}	Gaia Collaboration (2023)
ϖ	7.41 ± 0.04	mas	Gaia Collaboration (2023)
TYCHO B	7.861 ± 0.015	mag	Høg et al. (2000)
TYCHO V	7.775 ± 0.011	mag	Høg et al. (2000)
Gaia G	7.7481 ± 0.0028	mag	Gaia Collaboration (2023)
Gaia G_{BP}	7.7687 ± 0.0028	mag	Gaia Collaboration (2023)
Gaia G_{RP}	7.6794 ± 0.0038	mag	Gaia Collaboration (2023)
Gaia G_{RVS}	7.6387 ± 0.0051	mag	Gaia Collaboration (2023)
2MASS J	7.582 ± 0.019	mag	Cutri et al. (2003)
2MASS H	7.582 ± 0.036	mag	Cutri et al. (2003)
2MASS K_{s}	7.563 ± 0.023	mag	Cutri et al. (2003)
WISE $W1$	7.538 ± 0.028	mag	Wright et al. (2010)
WISE $W2$	7.583 ± 0.022	mag	Wright et al. (2010)
WISE $W3$	7.140 ± 0.017	mag	Wright et al. (2010)
WISE $W4$	4.210 ± 0.019	mag	Wright et al. (2010)
SPHERE $H2$	7.59 ± 0.03	mag	This work
SPHERE $H3$	7.58 ± 0.03	mag	This work
SPHERE $K1$	7.57 ± 0.02	mag	This work
SPHERE $K2$	7.56 ± 0.02	mag	This work
SpT	A0V		Houk (1982)
T_{eff}	9540 ± 100	K	This work
$\log g$	4.1 ± 0.1	dex	This work
[M/H]	$\lesssim 0.05$	dex	This work
R_*	1.50 ± 0.01	$R_\odot$	This work
A_V	0.21 ± 0.02	mag	This work
$\log L/L_\odot$	1.22 ± 0.01	dex	This work